Phys. Status Solidi B **253**, No. 1, 61–66 (2016) / **DOI** 10.1002/pssb.201552263

Part of Topical Section on
Polarization-field control in nitride light emitters

physica status solidi b
www.pss-b.com
basic solid state physics

Optimizing GaN (11$\bar{2}$2) hetero-epitaxial templates grown on (10$\bar{1}$0) sapphire

Markus Pristovsek*, **Martin Frentrup, Yisong Han, and Colin J. Humphreys**

Department of Materials Science and Metallurgy, University of Cambridge, 27 Charles Babbage Road, Cambridge, CB3 0FS, UK

Received 27 April 2015, revised 30 July 2015, accepted 31 July 2015
Published online 28 August 2015

Keywords basal plane stacking faults, MOVPE growth, semi-polar GaN, XRD

* Corresponding author: e-mail mp680@cam.ac.uk, Phone: +44-1223-331954

The hetero-epitaxy of (11$\bar{2}$2) GaN on (10$\bar{1}$0) sapphire was optimized in metal–organic vapor phase epitaxy. Best results were obtained from an AlN nucleation followed by AlN and AlGaN layers, and inserting low-temperature AlN interlayers (ILs) as well as a SiN_x IL. X-ray diffraction (XRD) of ω scans of the symmetric (11$\bar{2}$2) reflection yielded an ω FWHM <450″ along [11$\bar{2}\bar{3}$] and <900″ along [10$\bar{1}$0] together with a 100 × 100 μm^2 rms roughness below 10 nm as determined by atomic force microscopy. The lowest threading dislocation density achieved was ≈10^9 cm^{-2} while the basal plane stacking fault density was in the lower 10^5 cm^{-1} range as determined by transmission electron microscopy. The suppression of the unwanted (10$\bar{1}\bar{3}$) phase was lower than 1 in 10,000 as judged from XRD.

1 Introduction With its reduced spontaneous and piezoelectric fields, the semi-polar (11$\bar{2}$2) GaN is promising for the fabrication of green and yellow light-emitting diodes and normally-off field effect transistors. The (11$\bar{2}$2) orientation can be obtained by GaN epitaxy on *m*-plane (10$\bar{1}$0) sapphire substrates. But such templates have typically a huge density of dislocations in the 10^{10} cm^{-2} range and basal-plane stacking faults (BSFs) in the upper 10^5 cm^{-1} range [1–3]. Furthermore, contributions from the unwanted (10$\bar{1}\bar{3}$) phase have been observed [4, 5]. It has been shown that by inducing three dimensional (3D) growth, the peak width in X-ray diffraction (XRD) can be strongly reduced [2]. However, the 3D–2D growth technique results typically in rough surfaces. Also the sapphire miscut seems to have some influence on the surface roughness [6].

Different interlayer methods have been tried to reduce threading dislocations by promoting 3D growth. Exotic elements have been tried like ScN [7], CrN [8], as well as more common elements like InN quantum dots [9], or SiN_x interlayers [10, 11]. While these reduce XRD ω FWHM, they often lead to very rough surfaces.

Apart from threading dislocations and other defects, BSFs are important defects in non-(0001)-oriented growth. For the (10$\bar{1}\bar{3}$) orientation, these defects could be at least locally reduced by using low-temperature AlN interlayers, which strain the following GaN surface and hence reduce the chance for BSFs to continue [12]. To our knowledge, this technique has not been used in other orientations.

Finally, also other nucleation techniques like AlN nucleation have been employed [13, 14]. Since nucleation with AlN reduces the contributions of unwanted (10$\bar{1}\bar{3}$)-oriented grains [15, 16], subsequent GaN growth may lead to more phase pure substrates.

Our aim is to review these techniques and implement the best possible combination of layers for optimized hetero-epitaxial GaN templates on (10$\bar{1}$0) sapphire.

2 Experimental Growth was performed in a 6 × 2″ Aixtron close-coupled showerhead metal–organic vapor phase epitaxy (MOVPE) reactor. The growth process was monitored with a three wavelength Laytec EpiTT reflectometer.

Two different approaches have been used for the initial GaN buffer. One is a nucleation of GaN islands which were annealed and overgrown. This approach is described in Ref. [2]. The other approach is AlN nucleation, which

is performed at 5 kPa reactor pressure with a total flow of 21.7 L min^{-1}. First the reactor is heated to 1060 °C under hydrogen flow and 150 Pa of NH_3. After 90 s of temperature stabilization, the surface is nitridated with 700 Pa of NH_3 for 30 s. Then, ≈20 nm AlN is nucleated with 0.1 Pa tri-methyl aluminium (TMAl), 700 Pa NH_3. Nucleation is then stopped and the temperature is ramped to 1140–1200 °C (as high as possible) while reducing the NH_3 partial pressure to 160 Pa in 120 s. The final buffer of 95 nm AlN was grown for 700 s. In order to proceed from AlN toward GaN, a graded AlGaN layer is inserted by adding 0.07 Pa tri-methyl gallium (TMGa). The AlGaN layer was grown for 300 s while the TMGa is ramped up to 1.3 Pa and the temperature is ramped down to 1040 °C, leading to ≈150 nm of graded AlGaN. Then, TMGa and TMAl are switched off and the surface is annealed for 300 s for additional smoothing while NH_3 is ramped to 2000 Pa and the GaN buffer temperature is set to 1080 °C. For buffer growth, we use a rather higher growth rate of 1.4 nm s^{-1} (TMGa 2.3 Pa).

For a low-temperature AlN interlayer (IL), the GaN growth is interrupted and at ≈ 800 °C roughly 10 nm AlN is grown followed by 30 s (about 20–30 nm) AlGaN. The reactor pressure is 10 kPa, NH_3 is 230 Pa, TMAl is 0.08 Pa, and TMGa is ramped from 0 to 4.0 Pa. Growth is then stopped and all parameters are ramped back to buffer growth conditions.

For the SiN_x IL, we use a reduced NH_3 pressure of 350 Pa, and 3 mPa SiH_4 (from SiH_4 diluted to 500 ppm) for 125 s at 1000 °C, followed by ≈50 nm of GaN at lower growth rate and high V/III ratio to promote 3D growth. This low-temperature overgrowth is needed, since the SiN_x tends to be unstable at standard GaN growth conditions. Then, the temperature is ramped back to 1080 °C, and the following GaN is grown with a very high growth rate (1.5 nm s^{-1}) and low V/III ratio (<125) to enhance coalescence and smoothen the surface. Finally, the parameters are ramped to the standard GaN buffer layer conditions.

To investigate the effect of the different templates on the optical properties, we grow 5× InGaN quantum wells (QWs) with a thickness of 2.6 nm, an In content of (17 ± 1) %, and a barrier of 9 nm. The detailed properties of the QW are described elsewhere [17].

The samples were characterized by optical microscopy, room temperature photoluminescence (PL) mapping with a Q-switched laser emitting at 266 nm. Atomic force microscopy (AFM) was performed with a Digital Instrument 300 in tapping mode. Additionally, we attempted to count dark spots in room temperature plan-view cathodoluminescence images, which is only possible for densities below 10^9 cm^{-2}. On smooth samples pits could be distiguished in AFM, which correlated with the density of the dark pits. This method works up to densities of 10^{10} cm^{-2}.

We measured X-ray diffraction rocking curves of the (0006) and (20$\bar{2}$02) reflections in pure asymmetric geometry, the (11$\bar{2}$2) reflection in symmetric geometry, both perpendicular and parallel to the in-plane [1$\bar{1}$00] direction. In addition, ω–2Θ scans of the symmetric reflection were performed to investigate the phase purity of the material. To

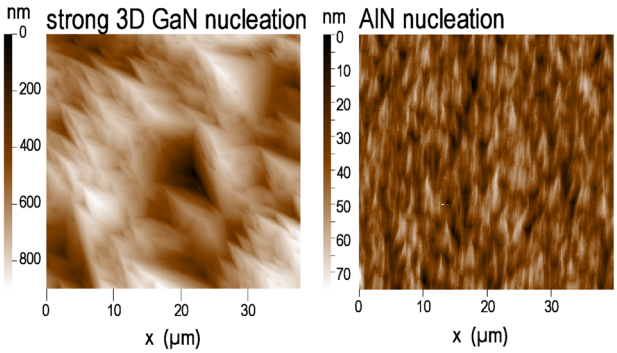

Figure 1 AFM scans of semi-polar templates with symmetric (11$\bar{2}$2) XRD ω FWHMs of 600″ along [11$\bar{2}\bar{3}$] and 1000″ along [1$\bar{1}$00]. The 3D GaN nucleation (left) has an rms roughness of 135 nm after ≈ 6 μm buffer growth, while the GaN sample grown with an AlN nucleation (right) has an rms roughness of 9.4 nm even though it included two AlN ILs and one SiN_x IL and is less than 2 μm thick.

determine the AlGaN composition, we used XRD measurements of the asymmetric (20$\bar{2}$5) reflection [18]. Finally, the BSF density was qualitatively investigated via diffuse X-ray scattering which broadens sensitive reflections perpendicular to the stacking faults, e.g., (h 0 $\bar{h}$ 0) with $h = 1$ or 2. This effect was demonstrated for non-polar (11$\bar{2}$0) GaN [19, 20]. However, for semi-polar (11$\bar{2}$2)-oriented samples, these reflections are not accessible. Therefore, we measured series of reciprocal space maps (RSMs) from BSF sensitive (20$\bar{2}l$) ($l = 1 \ldots 5$) reflections parallel to the [0001] direction (thus within the (11$\bar{2}$0) zone) as in Ref. [21].

The defect structure of the samples was investigated in a Philips CM30 transmission electron microscope (TEM). In particular, the BSF density of the samples was measured on plan-view TEM thin foils, which were tilted to establish a (1$\bar{1}$00) two-beam condition close to the [11$\bar{2}$0] zone axis, where all BSF are in contrast. The number of BSFs was then counted along [11$\bar{2}\bar{3}$] perpendicular to the BSFs.

3 Results and discussion There are two main ways of nucleating (11$\bar{2}$2) GaN on (10$\bar{1}$0) sapphire. The more common one uses a GaN nucleation procedure similar to that for (0001) GaN, i.e., first nitridation of sapphire at high temperature, then growth of a low-temperature GaN nucleation layer which is annealed and finally the GaN buffer layer. The latter may have first a 3D growth step with lower V/III ratios (<500) and lower temperatures (960–1020 °C), or the buffer may consist entirely of a smoothening step with higher temperatures (1020–1060 °C) and a higher V/III (>1000) ratio. This approach will be named 3D GaN nucleation. Depending on the 3D growth start, this approach can result in narrow XRD ω FWHMs at the price of very rough surfaces (Fig. 1 left) with an rms roughness larger than 100 nm (strong 3D in Table 1).

Reducing the degree of initial 3D GaN nucleation can yield smoother surfaces with roughness down to 10 nm. But then the XRD ω FWHM increases again (weak 3D in Ta-

Table 1 Typical XRD ω FWHM (given in arcsec) and AFM rms roughness for $100 \times 100\ \mu m^2$ using different nucleation and ILs. For comparison, the last row shows values reported in literature for $(11\bar{2}2)$ GaN on patterned $(10\bar{1}2)$ sapphire [31–34].

	(0006)	$(11\bar{2}2)$		XRD intensity	AFM $(100\ \mu m)^2$
	asymmetric	along $[11\bar{2}\bar{3}]$	along $[1\bar{1}00]$	$(11\bar{2}2)/(10\bar{1}\bar{3})$	rms (nm)
strong 3D GaN	500 ± 50	650 ± 100	1100 ± 100	100–250	>100
3D GaN	800 ± 200	1000 ± 100	1700	100–250	10
weak 3D GaN	800 ± 200	900 ± 100	1400	100–250	25
3D GaN+ILs	500 ± 50	650 ± 100	1200 ± 100	100–250	12–20
AlN	700 ± 50	1000 ± 100	1200 ± 100	>10, 000	8–10
AlN+ILs	430 ± 30	500 ± 50	900 ± 100	>10, 000	10–12
patterned	320	200–300	300–700	no $(10\bar{1}\bar{3})$	8–20

ble 1). Hence, we attempted another approach, with nucleation of AlN at high temperatures. The AlN nucleation immediately yields smooth surfaces (Fig. 1 right, Table 1) with very high Fabry–Pérot oscillations of the *in-situ* reflectance signal during growth (blue curve in Fig. 2) which are maintained for a long time. The 3D GaN nucleation instead starts at very low reflection values (red curve in Fig. 2) and hence never comes close to the expected mean value of 0.17 even after a long overgrowth. Moreover, using the AlN nucleation the whole template growth requires less than 2 h, and much less GaN is grown (less than 2 µm compared to more than 5 µm for 3D GaN nucleation). Hence, the AlN nucleation yield less bow after cooling to room temperature.

Figure 2 shows also another detail of the *in-situ* reflectance: the damping of the oscillations on the $(11\bar{2}2)$ orientation is not only due to roughness. The $(11\bar{2}2)$ orientation is a birefringent material in vertical incidence. As a result, the oscillation amplitude vanishes when the optical beam path of the extraordinary polarization differs by half a wavelength from the ordinary polarization. Subsequent growth increases the amplitude again with the phase shifted by 180° (black and red curves in Fig. 2). The literature for the refractive index difference at 633 nm suggests a $\Delta n = 0.045$ at room temperature [22, 23]. We observe a minimum on $(11\bar{2}2)$ (tilt angle to optical axis of 58°) at 1050 °C around 5.5 µm GaN thickness, which gives a $\Delta n = \lambda/(2d) = 0.06$. However, the larger value can be easily explained by the thermal red-shift of the GaN bandgap since Δn increases closer to the band edge [22].

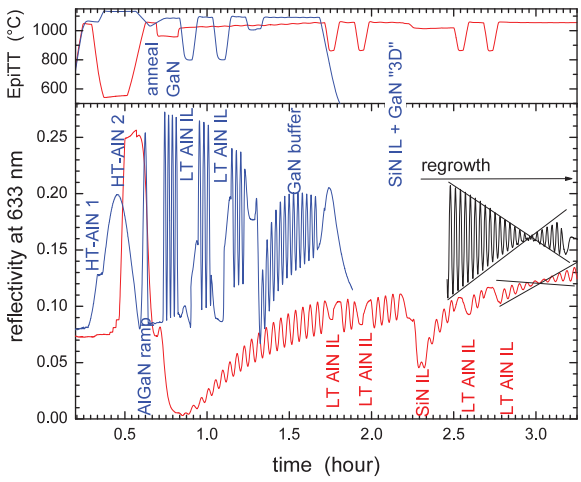

Figure 2 *In-situ* reflectance and pyrometry-corrected temperature for an optimized 3D GaN nucleation (red) and optimized AlN nucleation (blue), and the start of regrowth on this template (black, right). For thicker GaN layers, the vanishing and reappearing of the Fabry–Pérot oscillations are indicated by the envelope.

The XRD ω–2Θ scans with an open detector around the symmetric $(11\bar{2}2)$ reflection (parallel to $[1\bar{1}00]$) differ strongly for the two different nucleations. Figure 3 shows for the 3D GaN nucleation (black), a strong contribution of $(10\bar{1}\bar{3})$ GaN (ratio to $(11\bar{2}2)$ about 220) while for the AlN nucleation (red) a feature at 32.3° is hardly noticeable (intensity ratio larger than 10,000). Furthermore, the $(10\bar{1}\bar{3})$ reflection is strongly shifted compared to the expected position. One may speculate that this peak rather results from $(10\bar{1}\bar{3})$ AlGaN where residual GaN mixes with the AlN from the first nucleation step. Indeed, a thorough baking of the reactor before AlN nucleation can further reduce this feature.

The residual strain differs for both nucleation methods. Using GaN, it is very easy to relax compressive strain during 3D growth. Hence, the $(11\bar{2}2)$ reflection for the 3D GaN nucleation is at the expected position in Fig. 3. However, for the AlN nucleation, the $(11\bar{2}2)$ reflections for AlN and

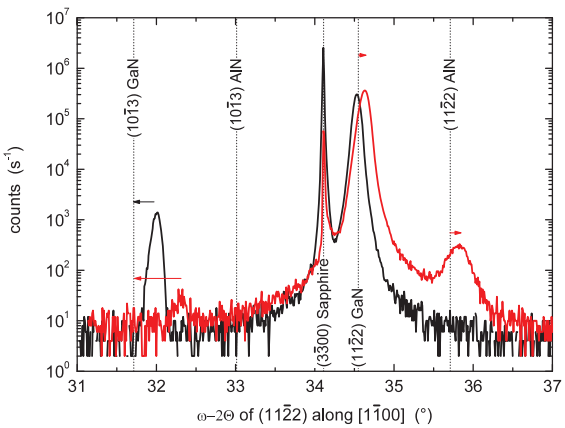

Figure 3 Symmetric XRD ω–2Θ scans with open detector around GaN $(11\bar{2}2)$ along $[1\bar{1}00]$ for 3D GaN nucleation (black) and with AlN nucleation (red).

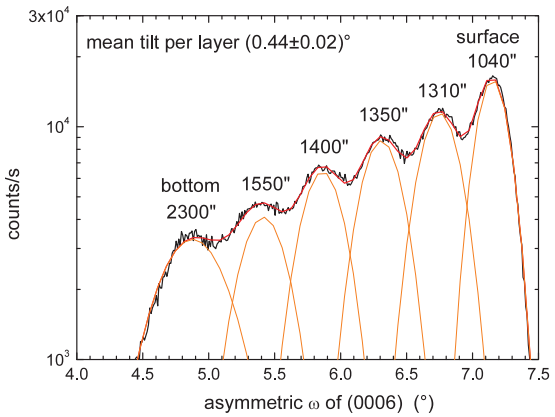

Figure 4 Asymmetric XRD ω scan around (0006) GaN along [11$\bar{2}\bar{3}$] direction for a sample containing five relaxed AlN ILs and a final thicker GaN capping. The intensity can be fitted nicely by multiple Gaussian functions. Each FWHM value (in arcsec) is given in the figure. (Note that the surface layer had more than twice the thickness of the others.)

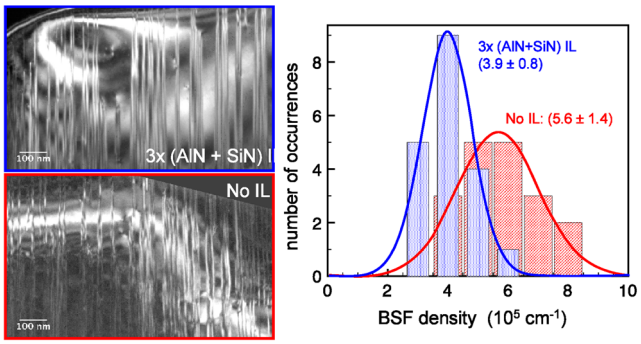

Figure 5 Plan-view TEM of a template produced by weak 3D GaN nucleation. It was then either overgrown with GaN inserted with three AlN ILs each followed by an SiN_x IL (top) or overgrown with a thick GaN layer only (bottom). The figure on the right shows the density of BSFs in the two samples (shaded red without ILs, blue with ILs).

GaN (11$\bar{2}$2) show a shift of 0.13° and 0.08°, respectively, toward larger angles (red arrows in Fig. 3). Since the AlN nucleation is performed at two different temperatures, one could expect some thermal residual strain from the second layer. Furthermore, the AlGaN and GaN layers on top are under tensile strain which cannot easily relax via 3D growth. One may speculate that the tensile strain promotes the flat surface typical for the AlN nucleation.

This behavior motivated us to introduce deliberately relaxed AlN ILs with some AlGaN on top to introduce additional tensile strain and help to further smoothen the GaN surface. The insertion of a relaxed low-temperature grown AlN IL results in a tilt along [0001] of the subsequent layer (Fig. 4). That is expected, since such a tilt is the easiest way to release strain for the semi-polar AlN. In Ref. [12], this effect was also assumed to influence the continuation of BSFs and ultimately reduce their density by a factor of four or five.

Figure 4 shows that the lattice tilting can be repeated many times. However, beyond two repeats no further significant improvement is seen in the surface smoothness (judged by *in-situ* optical reflectivity), and neither the RT PL intensity nor the XRD ω FWHM improves any further. (Note that the last layer in Fig. 4 had more than twice the thickness of the previous ones which contributed to the smaller ω FWHM.) This indicates that the AlN ILs also produce new defects (presumably at the GaN to AlN interface) which then gradually annihilate with increasing layer thickness. Therefore, and in order to avoid a highly tilted layer, we decided to use only two AlN interlayers.

SiN_x ILs have also been shown to reduce dislocations and BSFs in the growth of (11$\bar{2}$0) [24, 25] and (11$\bar{2}$2) [10] GaN templates. The SiN_x IL induces islanding and subsequent 3D growth, similar to observed for the growth of (0001) GaN, e.g., [26, 27]. The 3D growth on (11–22) induced by the SiN_x IL was seen by AFM [10] and is also clearly visible in the *in-situ* optical reflectance transient in Fig. 2 by the reduction of the signal at 1.3 h for AlN nucleation and 2.3 h for 3D GaN nucleation. But the SiN_x IL can also cause a too strong 3D growth which again leads to a very rough surface. Hence, the Si exposure must be carefully adjusted in order to achieve just enough 3D growth for defect reduction, but ensure that a smooth surface can be still recovered after overgrowth. Compared to (0001), the (11$\bar{2}$2) surface only needs about half of the amount of SiN_x at similar growth conditions to induce strong 3D growth. However, a more detailed study of the structure of SiN_x IL on (11$\bar{2}$2) GaN is currently ongoing [28].

Figure 5 shows the effect of three pairs of AlN and SiN_x ILs on the BSF density as measured by plan-view TEM. The spacing between BSFs increases on the samples with ILs, i.e., the BSF density is nearly halved. In practice, one SiN_x IL is sufficient; more can even increase the defect density again and lead to severe roughening of the surface.

Since BSF density analysis by TEM is time consuming, we tried to obtain density information on BSFs directly from XRD. Figure 6 shows a series of RSMs of the (20$\bar{2}l$) reflection ($l = 1 \ldots 4$) for a sample with AlN nucleation without ILs. Parallel to [0001] is a clear streak which connects the reflections. This is caused by diffuse scattering from the BSFs. In samples with ILs, or using epitaxial lateral overgrowth (ELOG), this diffuse scattering is reduced. It is entirely suppressed for patterned substrates with BSF densities below 500 cm^{-1} (cf. [29]), and similar for patterned (10$\bar{1}$2) sapphire where BSFs are below 1000 cm^{-1} [31–34]. This is better seen in the bottom graph of Fig. 6. The intensity at the higher Q values (to the right side) is clearly correlated with the BSF density, i.e., the higher diffuse scattering, the more BSFs. However, quantitative modeling by simulating the different shapes is still under way, following recent works on (11$\bar{2}$2) GaN [21].

However, even better hetero-epitaxial templates have dislocation densities in the low 10^9 cm^{-3} region (as determined from pits in AFM). With such a high number of dislocations, not only the BSFs are reducing light emission at room temperature. Figure 7 clearly demonstrates that all kind of defects

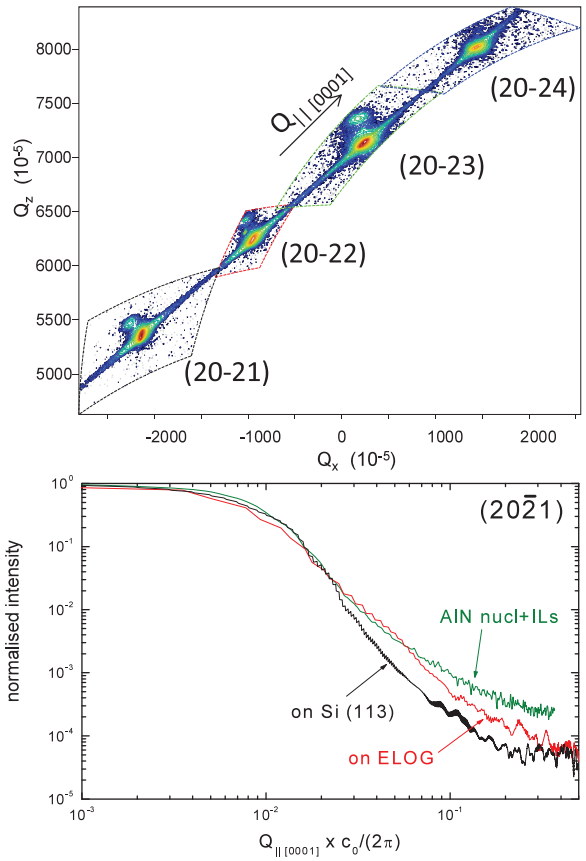

Figure 6 Top shows an RSM map from the (20$\bar{2}$1) to (20$\bar{2}$4) reflection in the (11$\bar{2}$0) plane of a sample with AlN nucleation but no ILs. Bottom shows the extracted intensity of the (20$\bar{2}$1) peak along the streak in [0001] for three different samples with comparable ω FWHM, black on patterned (113) Si [29] (BSF 500 cm^{-1}), using ELOG [30] (BSF 10^3-10^4 cm^{-1}), and for AlN nucleation with ILs (BSF low 10^5 cm^{-1}).

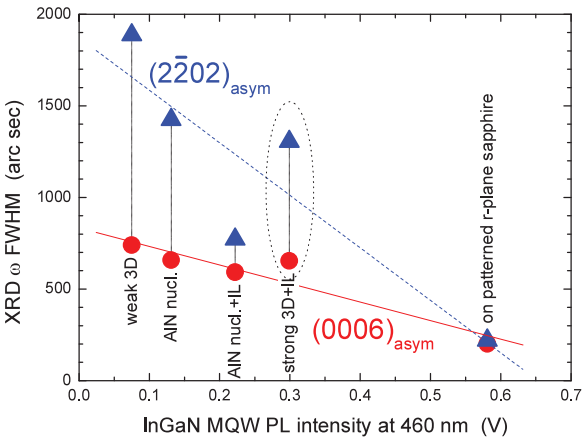

Figure 7 PL peak signal intensity of 5× InGaN QWs around 465 nm versus the XRD ω FWHM of the asymmetric (0006) and the asymmetric (2$\bar{2}$02). The QWs were grown simultaneously on various templates together with an (0001) sample. The patterned template had less than 500 cm^{-1} BSF and less than 10^8 cm^{-2} dark spots in CL [32]. The (0001) sample (not shown) had a PL intensity of 2.4 V.

can reduce the PL signal. Especially, the ω FWHM of the asymmetric (0006) reflection correlates nicely with the peak PL signal of a 5× InGaN QW around 465 nm. However, the surface roughness also affects the PL intensity, since a higher roughness can easily increase the light out-coupling by a factor of three. This is most likely the reason why the sample with strong 3D GaN nucleation (dotted circle in Fig. 7) emits more light despite having a wider XRD ω FWHM. Nevertheless, QWs on hetero-epitaxial templates gave at best a third of the PL intensity compared to QWs grown on GaN templates on patterned *r*-plane sapphire, which can reach closer or even below 10^8 cm^{-3} defects [31–33].

Table 1 summarizes the XRD and AFM data that can be achieved using the various approaches discussed in this work and compared them to typical results on patterned substrate from Refs. [31–34]. Overall, the method using AlN nucleation combines a narrow XRD ω FWHM with a smooth surface. Furthermore, it is a reproducible growth process, unlike 3D GaN nucleation, which depends strongly on the coating of the susceptor. Compared to previous investigations, an XRD ω FWHM along [11$\bar{2}\bar{3}$] for the (11$\bar{2}$2) reflection of less than 500″ has been achieved only with ScN ILs [7] or approaches in which patterned substrates are used while hetero-epitaxial AlN nucleation as well as AlN and SiN_x ILs can be grown in almost any MOVPE reactor without the need for prior lithography and patterning.

4 Conclusions We have investigated and evaluated several MOVPE growth methods to obtain (11$\bar{2}$2) GaN templates hetero-epitaxially grown on sapphire substrates. The method using AlN nucleation at higher temperatures, followed by a graded AlGaN layer and thermal annealing allowed for very smooth GaN layers at a relatively thin total layer thickness. Further surface smoothing and defect reduction can be achieved via the inclusion of relaxed AlN ILs and a SiN_x IL, the latter by inducing 3D growth. While we could achieve XRD ω FWHMs in the 450″ range perpendicular and 900″ in [1$\bar{1}$00] direction, these are still a factor of 2–3 broader than for (11$\bar{2}$2) GaN templates on patterned substrates. Hence, the PL intensity from InGaN QWs was less than half of that obtained for similar structures grown on patterned substrates.

Supporting Information Additional supporting information may be found in the online version of this article at the publisher's website.

Acknowledgements This work was supported by EU-FP7 ALIGHT No. NMP-2011-280587 and the UK Engineering and Physical Sciences Research Council No. EP/I012591/1 and EP/J003603/1.

References

[1] T. J. Baker, B. A. Haskell, F. Wu, J. S. Speck, and S. Nakamura, Jpn. J. Appl. Phys. **45**(2L), L154 (2006).
[2] M. J. Kappers, J. L. Hollander, C. McAleese, C. F. Johnston, R. F. Broom, J. Barnard, M. Vickers, and C. J. Humphreys, J. Cryst. Growth **300**(1), 155 (2007).

[3] S. Jang, H. Kim, D. Soo Kim, S.-M. Hwang, J. Kim, and K. Hyeon Baik, Appl. Phys. Lett. **103**, 16, 162103 (2013).
[4] S. Ploch, M. Frentrup, T. Wernicke, M. Pristovsek, M. Weyers, and M. Kneissl, J. Cryst. Growth **312**, 2171 (2010).
[5] S. Ploch, J. B. Park, J. Stellmach, T. Schwaner, M. Frentrup, T. Niermann, T. Wernicke, M. Pristovsek, M. Lehmann, and M. Kneissl, J. Cryst. Growth **331**, 25 (2011).
[6] S. Bae, D. Lee, B. Kong, H. Cho, J. Kaeding, S. Nakamura, S. DenBaars, and J. Speck, Curr. Appl. Phys. **11**(3), 954 (2011).
[7] M. A. Moram, C. F. Johnston, M. J. Kappers, and C. J. Humphreys, J. Cryst. Growth **311**(12), 3239 (2009).
[8] K.-W. Liu, S.-J. Chang, S.-J. Young, T.-H. Hsueh, H. Hung, Y.-C. Mai, S.-M. Wang, and Y.-Z. Chen, J. Electrochem. Soc. **158**(10), H983 (2011).
[9] C. Jung, J. Jang, J. Hwang, J. Jeong, J. Kim, K. Lee, and O. Nam, J. Cryst. Growth **370**, 26 (2013).
[10] J. Jeong, J. Jang, J. Hwang, C. Jung, J. Kim, K. Lee, H. Lim, and O. Nam, J. Cryst. Growth **370**, 114 (2013).
[11] M. Ueno, Y. Hashimoto, K. Yamane, N. Okada, and K. Tadatomo, Phys. Status Solidi C **11**(3–4), 557 (2014).
[12] J. Bläsing, V. Holý, A. Dadgar, P. Veit, J. Christen, S. Ploch, M. Frentrup, T. Wernicke, M. Kneissl, and A. Krost, J. Phys. D **46**(12), 125308 (2013).
[13] Q. Sun, B. Leung, C. D. Yerino, Y. Zhang, and J. Han, Appl. Phys. Lett. **95**(23), 231904 (2009).
[14] K. Xing, Y. Gong, X. Yu, J. Bai, and T. Wang, Jpn. J. Appl. Phys. **52**(8S), 08JC03 (2013).
[15] J. Stellmach, M. Frentrup, F. Mehnke, M. Pristovsek, T. Wernicke, and M. Kneissl, J. Cryst. Growth **355**(1), 59 (2012).
[16] N. Hatui, M. Frentrup, A. A. Rahman, A. Kadir, S. Subramanian, M. Kneissl, and A. Bhattacharya, J. Cryst. Growth **411**, 106 (2015).
[17] M. Pristovsek, Y. Han, T. Zhu, C. J. Humphreys, D. Tytko, P.-P. Choi, D. Raabe, F. Brunner, and M. Weyers, Appl. Phys. Lett., submitted (2015).
[18] D. J. Wallis, D. Zhu, F. Oehler, S. P. Westwater, A. Pujol, and C. J. Humphreys, Semicond. Sci. Technol. **28**(9), 094006 (2013).
[19] M. A. Moram, C. F. Johnston, J. L. Hollander, M. J. Kappers, and C. J. Humphreys, J. Appl. Phys. **105**(11), 113501 (2009).
[20] M. Barchuk, V. Holý, D. Kriegner, J. Stangl, S. Schwaiger, and F. Scholz, Phys. Rev. B **84**, 094113 (2011).
[21] S. Bauer, S. Lazarev, M. Bauer, T. Meisch, M. Caliebe, V. Holý, F. Scholz, and T. Baumbach, J. Appl. Crystallogr. **48**(4), 1000 (2015).
[22] M. J. Bergman, Ü. Özgür, J. H. C. Casey, H. O. Everitt, and J. F. Muth, Appl. Phys. Lett. **75**(1), 67 (1999).
[23] N. A. Sanford, L. H. Robins, A. V. Davydov, A. Shapiro, D. V. Tsvetkov, A. V. Dmitriev, S. Keller, U. K. Mishra, and S. P. DenBaars, J. Appl. Phys. **94**(5), 2980 (2003).
[24] J. H. Kim, S.-M. Hwang, Y. G. Seo, K. H. Baik, and J. H. Park, Semicond. Sci. Technol. **28**(8), 085007 (2013).
[25] D. Sutherland, F. Oehler, T. Zhu, J. T. Griffiths, T. J. Badcock, P. Dawson, R. M. Emery, M. J. Kappers, C. J. Humphreys, and R. A. Oliver, Phys. Status Solidi C **11**(3–4), 541 (2014).
[26] H. Lahrèche, P. Vennéguès, B. Beaumont, and P. Gibart, J. Cryst. Growth **205**(3), 245 (1999).
[27] M. Kappers, R. Datta, R. Oliver, F. Rayment, M. Vickers, and C. Humphreys, J. Cryst. Growth **300**(1), 70 (2007).
[28] Y. Han, M. Pristovsek, T. Zhu, C. J. Humphreys, D. Tytko, P.-P. Choi, D. Raabe, L. Lymperakis, and J. Neugebauer, Phys. Rev. B, to be submitted (2015).
[29] M. Pristovsek, Y. Han, T. Zhu, M. Frentrup, M. J. Kappers, C. J. Humphreys, G. Kozlowski, P. Maaskant, and B. Corbett, Phys. Status Solid B **252**(5), 1104 (2015).
[30] T. Zhu, C. F. Johnston, M. J. Kappers, and R. A. Oliver, J. Appl. Phys. **108**(8), 083521 (2010).
[31] N. Okada, A. Kurisu, K. Murakami, and K. Tadatomo, Appl. Phys. Express **2**(9), 091001 (2009).
[32] F. Brunner, U. Zeimer, F. Edokama, W. John, D. Prasai, O. Krüger, and M. Weyers, Phys. Status Solidi B **252**(5), 1189 (2015).
[33] F. Tendille, P. D. Mierry, P. Vennégèus, S. Chenot, and M. Teisseire, J. Cryst. Growth **404**, 177 (2014).
[34] F. Scholz, T. Meisch, M. Caliebe, S. Schörner, K. Thonke, L. Kirste, S. Bauer, S. Lazarev, and T. Baumbach, J. Cryst. Growth **405**, 97 (2014).

